Infrasound from giant bubbles during explosive submarine eruptions

John J. Lyons [1]*, Matthew M. Haney[1], David Fee[2], Aaron G. Wech[1] and Christopher F. Waythomas[1]

Shallow submarine volcanoes pose unique scientific and monitoring challenges. The interaction between water and magma can create violent explosions just below the surface, but the inaccessibility of submerged volcanoes means they are typically not instrumented. This both increases the risk to marine and aviation traffic and leaves the underlying eruption physics poorly understood. Here we use low-frequency sound in the atmosphere (infrasound) to examine the source mechanics of shallow submarine explosions from Bogoslof volcano, Alaska. We show that the infrasound originates from the oscillation and rupture of magmatic gas bubbles that initially formed from submerged vents, but that grew and burst above sea level. We model the low-frequency signals as overpressurized gas bubbles that grow near the water–air interface, which require bubble radii of 50–220 m. Bubbles of this size and larger have been described in explosive subaqueous eruptions for more than a century, but we present a unique geophysical record of this phenomenon. We propose that the dominant role of seawater during the effusion of gas-rich magma into shallow water is to repeatedly produce a gas-tight seal near the vent. This resealing mechanism leads to sequences of violent explosions and the release of large, bubble-forming volumes of gas—activity we describe as hydrovulcanian.

Shallow explosive subaqueous eruptions, with vents less than 100 m below the surface[1], are poorly understood due to the difficulty of collecting data near submerged vents in remote locations[2–4]. Most insights into eruption dynamics at these systems have come from studies of eruptive products[5–8], analogue experiments and numerical modelling[9–11], and eyewitness accounts[12–14]. The limited geophysical observations, primarily from distal hydroacoustic and seismic data, lack the resolution to constrain the source mechanisms[4,15,16]. Much of what is known about the physics of underwater explosions comes from the analysis of chemical and nuclear explosions[9,17,18], which are used as eruption analogues in the absence of direct observations. Hydroacoustic waves and scaling laws related to the depth and size of underwater explosions have been studied extensively, but the associated atmospheric waves have received little attention. Low-frequency sound (<20 Hz), or infrasound, generated in the atmosphere can preserve eruption source information across long distances[19,20], but the source physics that generates infrasound from subaqueous eruptions remains poorly constrained due to observational limitations and environmental complexity. The strong density contrast between air and water should limit the acoustic transmission for submerged sources, yet low-frequency sound waves with wavelengths greater than the water depth can efficiently cross the interface[21,22]. Infrasound recorded over 1,500 km from the 2010 South Sarigan eruption was attributed to the subaerial cloud, despite the vent being at least 200 m below sea level[4].

Prior to the 2016–2017 eruption of Bogoslof volcano, Alaska, detailed infrasound from an explosive submarine eruption had not been captured. Here we present infrasound data recorded during the Bogoslof eruption and show that it is dominated by low-frequency signals with distinct, repetitive waveforms that indicate a consistent source mechanism. The waveforms share some diagnostic characteristics with infrasound produced by gas bubbles expanding and bursting at the magma–air interface during strombolian activity[23–26]. We present evidence that submarine explosions can produce infrasound through the growth, collapse and rupture of large bubbles near the water–air boundary, and show that these signals may be broadly indicative of the shallow subaqueous effusion of gas-rich magma.

Infrasound from the submarine eruption of Bogoslof

Bogoslof is a mostly submarine stratovolcano located 45 km northwest of the main trend of the Aleutian volcanic arc (Fig. 1a). The edifice rises 1,700 m above the floor of the Bering Sea, but the only surface expression of the large edifice, prior to the 2016–2017 eruption, was several low-elevation, erosion-resistant lava domes and pyroclastic deposits from historical eruptions. From December 2016 to August 2017, a shallow submarine eruption produced at least 70 periods of detected explosive activity and sent volcanic clouds as high as 12 km above sea level[27]. The clouds disrupted local and international air traffic for months, and on several occasions resulted in trace ash fall on local communities southeast of the volcano[27]. Eruptions emitted numerous SO_2 and ash clouds detected in satellite data, and generated abundant volcanic lightning and thunder[28]. Satellite and aircraft observations indicate that the vent area was submerged during most of the explosive eruptions (Fig. 1b,c). Water depths above the vent were likely in the 5–100 m range based on the National Oceanic and Atmospheric Administration and National Centers for Environmental Information bathymetry for the area (https://maps.ngdc.noaa.gov/viewers/bathymetry/) and satellite images retrieved after several eruptions.

Local monitoring stations did not exist on Bogoslof Island prior to or during the eruption because of its remote location and small subaerial landmass (0.3 km²). The infrasound sensors closest to Bogoslof are located 59 km south on Okmok volcano (Fig. 1a) and here we analyse data from this array. We focus on 262 discrete infrasound signals recorded during 8 explosive eruptions that occurred between 9 January and 10 July 2017 (Methods). Despite changes in vent location and island morphology, the eruptions produced
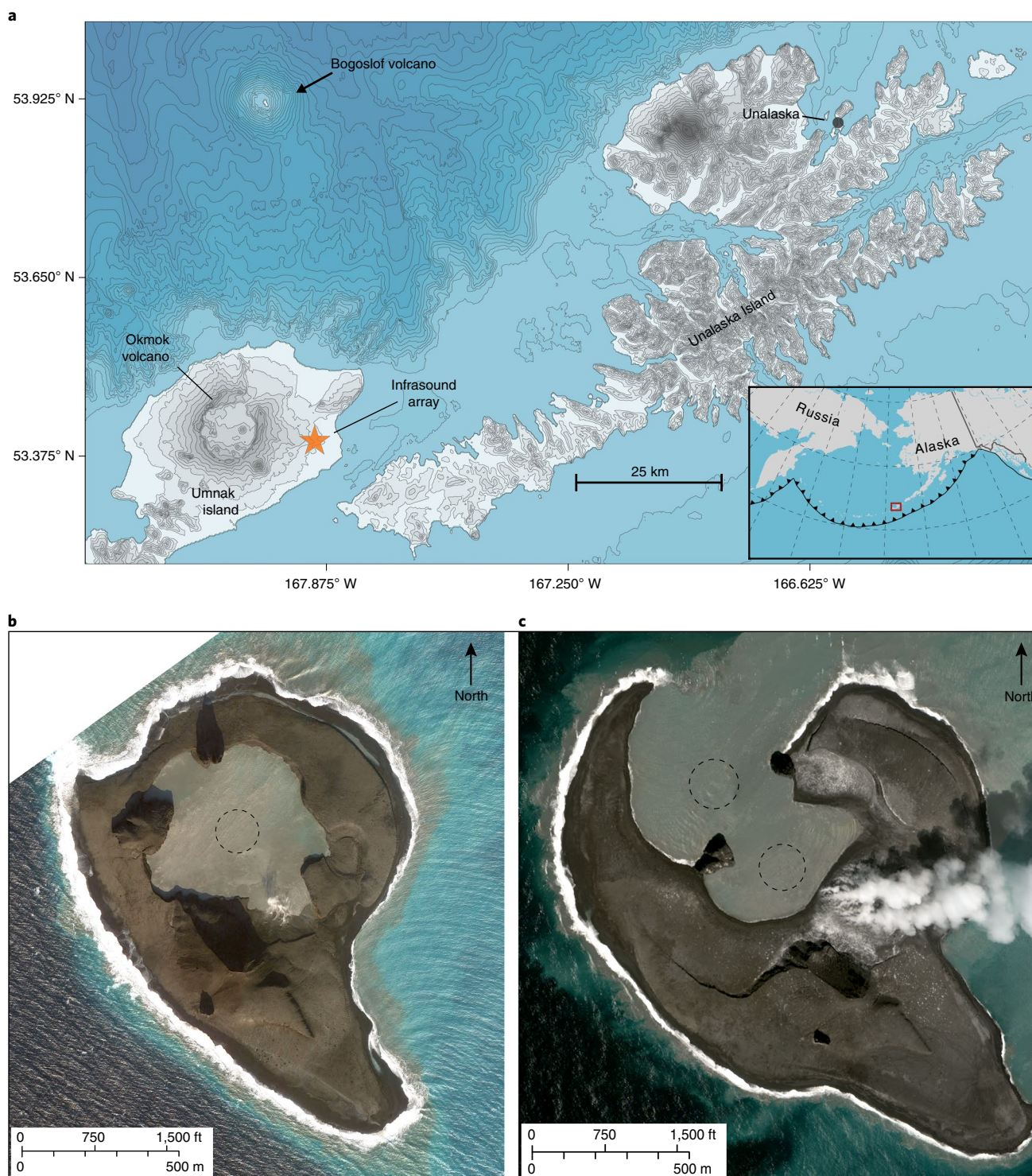
Fig. 1 | Map of Bogoslof volcano and two satellite images of the partially submerged summit and crater during the eruption. a, Location map of the Aleutian Arc (inset) and Bogoslof volcano, located northwest of the main trend of the arc in the Bering Sea. The orange star indicates the location of the OKIF infrasound array. **b,c**, WorldView satellite images of the subaerial portion of the vent region of Bogoslof near times when the bubble signals were recorded. Dashed lines circle the approximate submarine vent areas. WorldView data provided under the DigitalGlobe NextView License.

sequences of similar waveforms over many months that suggest a repetitive source mechanism. One of the most distinguishing characteristics of the Bogoslof eruption infrasound is its low-frequency content. For many of the eruptions the infrasound energy is concentrated in the 0.1 to 1 Hz band, with peak frequencies between 0.12 and 0.4 Hz (Fig. 2a). Higher frequencies, however, are not completely absent; many of the discrete events contain weak high-frequency components (Fig. 2a), and several eruptions show energetic broadband signals up to the Nyquist frequency (50 Hz). We manually selected waveforms from the instrument-corrected continuous data following automatic detections of coherent signals from the direction of Bogoslof using least-squares beamforming[29].
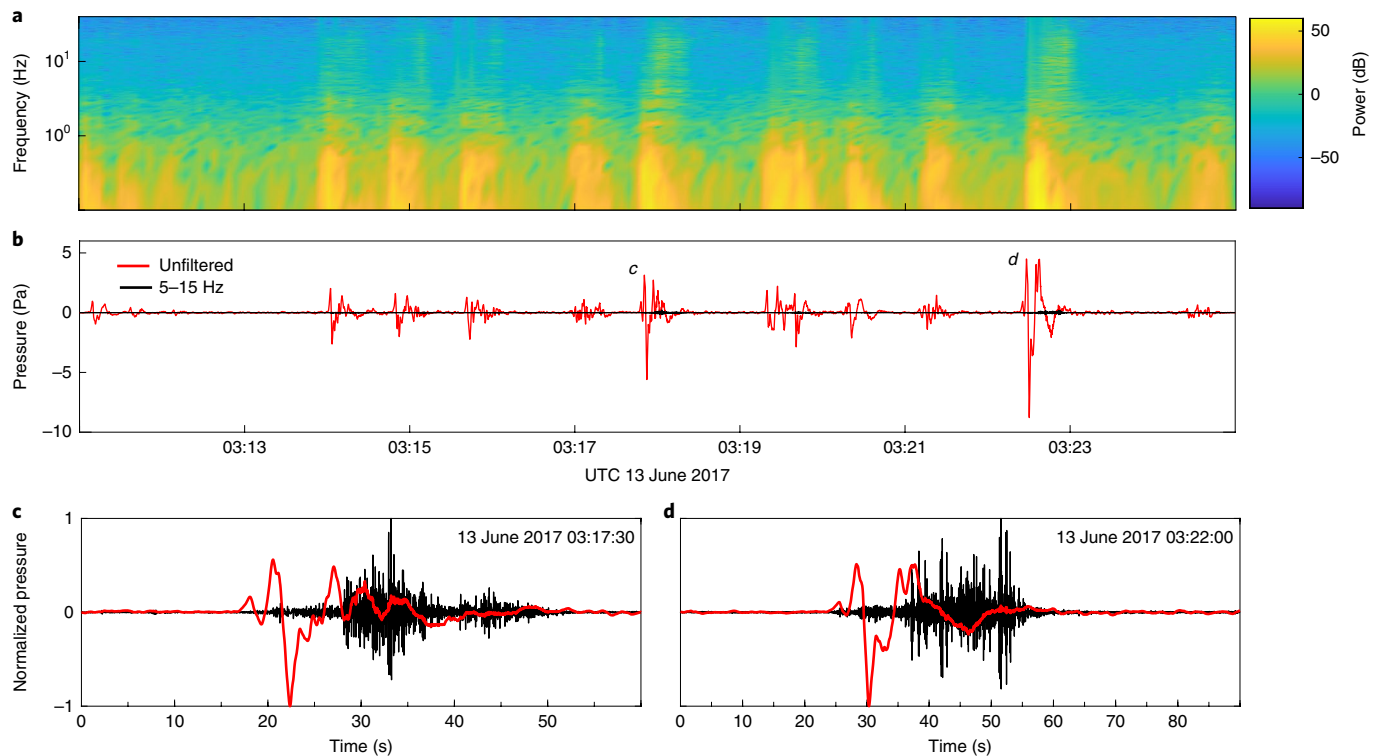
Fig. 2 | Infrasound signals from an explosive eruption of Bogoslof on 13 June 2017. a, Spectrogram of an unfiltered, 14 min infrasound trace that highlights the low-frequency character of the signal. **b**, Waveforms from **a**. The red trace is unfiltered and shows numerous discrete events separated by relative quiescence. The black trace is filtered from 5 to 15 Hz and emphasizes the lack of high-frequency energy produced. **c,d**, Windows around the two highest-amplitude events from **a** and **b**. The amplitudes of the data in **b** were normalized to reveal that the high-frequency signal amplitude increases at the end of the first low-frequency oscillation. UTC, coordinated universal time.

The 262 representative events occurred with high signal-to-noise ratios and when the rate of activity allowed pressure to return to background levels between events. The waveforms are similar to records of strombolian explosions, but with lower dominant frequencies (0.12–0.4 Hz) than typically recorded (0.5–10 Hz) during strombolian activity[30,31]. Filtering out the low-frequency energy revealed discernible high-frequency energy associated with only the highest-amplitude events (Fig. 2b).

We normalized the amplitude and plotted the high-frequency (5–15 Hz) bandpass-filtered signal together with the unfiltered signal for the two most energetic events of the 13 June 2017 eruption to highlight the relationship between the high-amplitude, low-frequency signals and the low-amplitude, high-frequency signals (Fig. 2c,d). High-frequency energy accompanies the onset of the low-frequency signals, but the amplitude of the high-frequency signal remains relatively low for the first 8–10 seconds until near the end of the main low-frequency pulse. At this point, the amplitude of the high-frequency signal increases rapidly and remains elevated for 10–20 seconds before decreasing in concert with the low-frequency signal as the event ends.

Sources of infrasound from submerged volcanic explosions

Volcanic explosions in magma at or near the surface produce infrasound, and several of the subaerial source models for the atmospheric accelerations that produce infrasound could also apply to volcanic explosions in shallow water. One of the simplest models is the isotropic expansion and burst of a pressurized volume in the atmosphere[32,33]. The burst of a spherical source produces simple waveforms with just a single compression–expansion cycle. The period of the resulting waveform is a function of the radius of the sphere and the sound speed (Methods). For Bogoslof signals with

8 second periods, the model predicts a sphere of 1,400 m radius, which is unrealistic given the size of the Bogoslof crater (Fig. 1). This model has been applied to short-duration strombolian[34,35] and vulcanian[36] explosions because it provides a means to estimate explosion mass flux and cumulative gas emissions[37]; however, it relies on several simplifying assumptions that can limit its use (Methods). Application of this technique to the low-frequency component of the Bogoslof infrasound (Methods) does not explain the waveform shape, as the large rarefaction that dominates the low-frequency signal (Figs. 2 and 3) results in an unrealistic negative volume flux (Supplementary Figs. 2 and 3). Ichihara et al.[9] also explored the ability of an expanding volume on the surface of the water to generate airwaves, but found that the calculated volume expansion of the surface over a shallow chemical explosion poorly matched the surface volume expansion from high speed-video. An explosion that occurs in shallow water could also produce long-period standing waves, or seiche[38], capable of generating infrasound signals from the displacement of large volumes of air[39]. The Bogoslof crater dimensions and average water depth would produce a seiche with a dominant period in the 20–100 second range, much longer than the longest-period eruption infrasound from Bogoslof (Methods).

A sequence of high-amplitude, low-frequency infrasound that preceded low-amplitude, high-frequency infrasound similar to the Bogoslof signals was observed during discrete explosions at Stromboli volcano[33]. In this case, the explanation for the frequency–amplitude sequence is that the low-frequency signal results from the oscillation of the shell of a metre-scale gas bubble at the magma–air interface prior to bursting and that the subsequent high-frequency energy is related to the bubble bursting and venting. Vergniolle and Brandeis[25,33] modelled the low-frequency component of the infrasound as the volumetric oscillation of a gas slug near the surface,

support this model[40]. Analogue experiments of bubble behaviour show that the liquid viscosity fundamentally controls whether or not the bubble oscillates, with the oscillation limited to experimental runs in which the liquid viscosity is low[41]. The bubble oscillation model of Vergniolle and Brandeis[25,33] builds on models and observations of gas bubbles oscillating at the air–water boundary as an efficient source of sound in the air[42–44]. We propose that the frequency–amplitude character and waveform repetition of the discrete Bogoslof infrasound events is the result of large bubbles formed by shallow submarine explosions that oscillate at the water–air interface, and subsequently rupture and vent into the atmosphere. The low viscosity of the water that overlies the vent at Bogoslof allows the large gas bubbles to oscillate prior to bursting.

Infrasound from a large bubble

Numerous compelling and detailed accounts of shallow subaqueous eruptions exist and share many common features suggesting similar source mechanics. Shallow subaqueous explosive events are frequently described as beginning with a doming or swelling of the water surface that grows over several seconds to a dark, often black, hemisphere that expands radially into the atmosphere before being disrupted by multiple jets of tephra, steam and water[12,13,45,46]. The resulting volcanic clouds continue to grow, sometimes reaching multiple kilometres above sea level over tens of minutes. Descriptions of the sizes of the initial explosion bubbles are mostly qualitative (for example, large, gigantic), but estimates range up to 450–500 m in diameter[12,13]. Previous historic eruptions of Bogoslof have been observed locally by passing ships[47]; witnesses on a nearby ship described repeated "gigantic dome-like swelling, as large as the US Capitol dome at Washington [DC]" (29 m in diameter) during the 1908 eruption[48]. This type of observation was not possible during the 2016–2017 eruption due to weather and safety concerns, so no visual observations of the events analysed here exist. Instead, we estimated the bubble size by comparing the infrasound signals described above to synthetic acoustic waves produced by modelling the oscillations of a large pressurized bubble at the water–atmosphere interface.

A pressurized gas bubble in an infinite liquid is easily excited into volume oscillation around its equilibrium size. Inertia results in the bubble overshooting the equilibrium radius, which causes underpressurization of the gas and bubble contraction. Compressibility of the gas provides a restoring force in the volume, which results in oscillation[32,43]. The oscillation can be considered as a monopole acoustic source (Methods), which radiates energy isotropically and efficiently into the far field with amplitude decreasing inversely with distance[32]. A sufficiently large bubble growing from a shallowly submerged vent will reach the surface and expand into the atmosphere (Fig. 4). Once the bubble has reached the surface, the viscosity and density contrast between air and water favours the expansion and oscillation of the thin hemispherical shell of water in the atmosphere rather than the motion of the submerged portion of the bubble[25]. The non-linear response of a gas bubble in an incompressible fluid to a time-varying pressure field can be modelled with the Rayleigh–Plesset equation[42], and here we follow a modified approach[25] to describe the bubble motion close to an air–water interface. A simplifying assumption in this method is that the model bubble exists near the air–water interface, and at time $t = 0$ is given an overpressure that results in its volumetric oscillation around the equilibrium size (Methods). It is this oscillation that is responsible for the main low-frequency infrasound signal in Fig. 2. The initial gas release and rapid growth of the bubble to its equilibrium size are complex and beyond the reach of this study.

We calculated 10^6 unique synthetic pressure waveforms by varying the values of bubble overpressure ΔP, the starting radius of the bubble R_o, the depth of the water above the vent D and the starting thickness of the fluid layer that forms the bubble cap h_{eq}
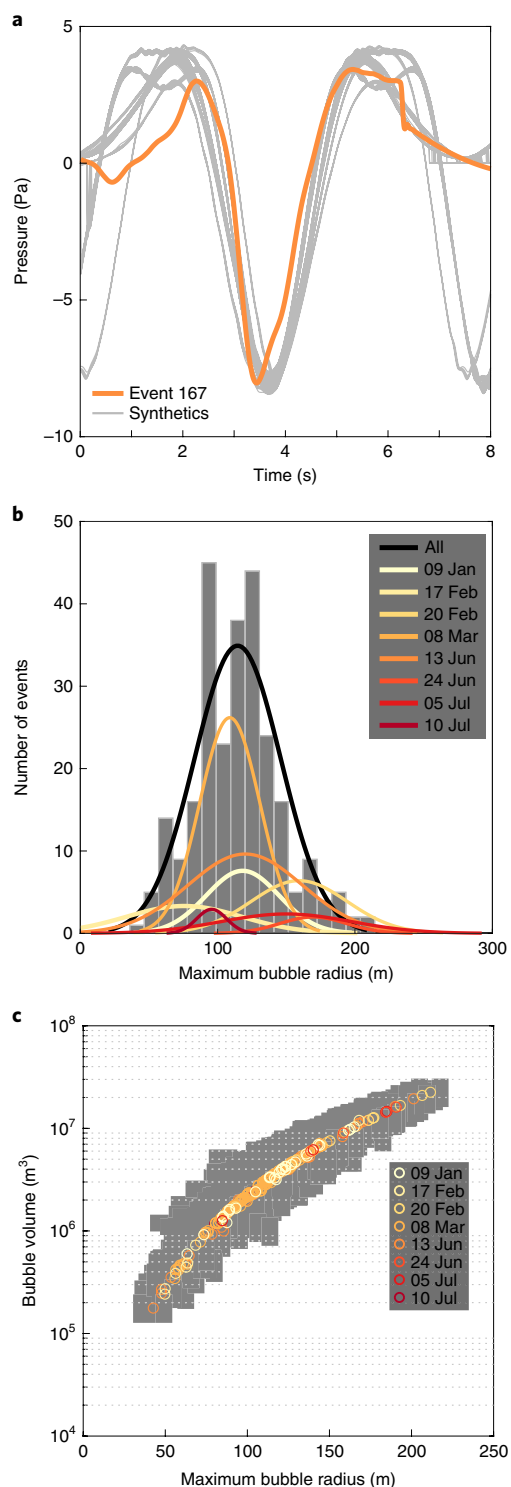
Fig. 3 | Results from modelling the Bogoslof infrasound signals as bubble oscillations. a, Low-frequency signal from event 167 (8 March 2017) and the 209 synthetic pressure traces that are within ±5% of the signal peak-to-peak pressure and dominant frequency. All the traces were aligned by cross-correlation. **b**, Distribution of the maximum bubble radii for events from the individual eruptive periods and all the events. **c**, Maximum bubble radii versus bubble volumes for the events studied. The grey field outlines values of 1 s.d. for both radius and volume.

which provided constraints on the bubble size and volume. Video and infrasound records of metre-scale bubbles deforming at the surface of the low-viscosity lava lake at Erta 'Ale volcano also
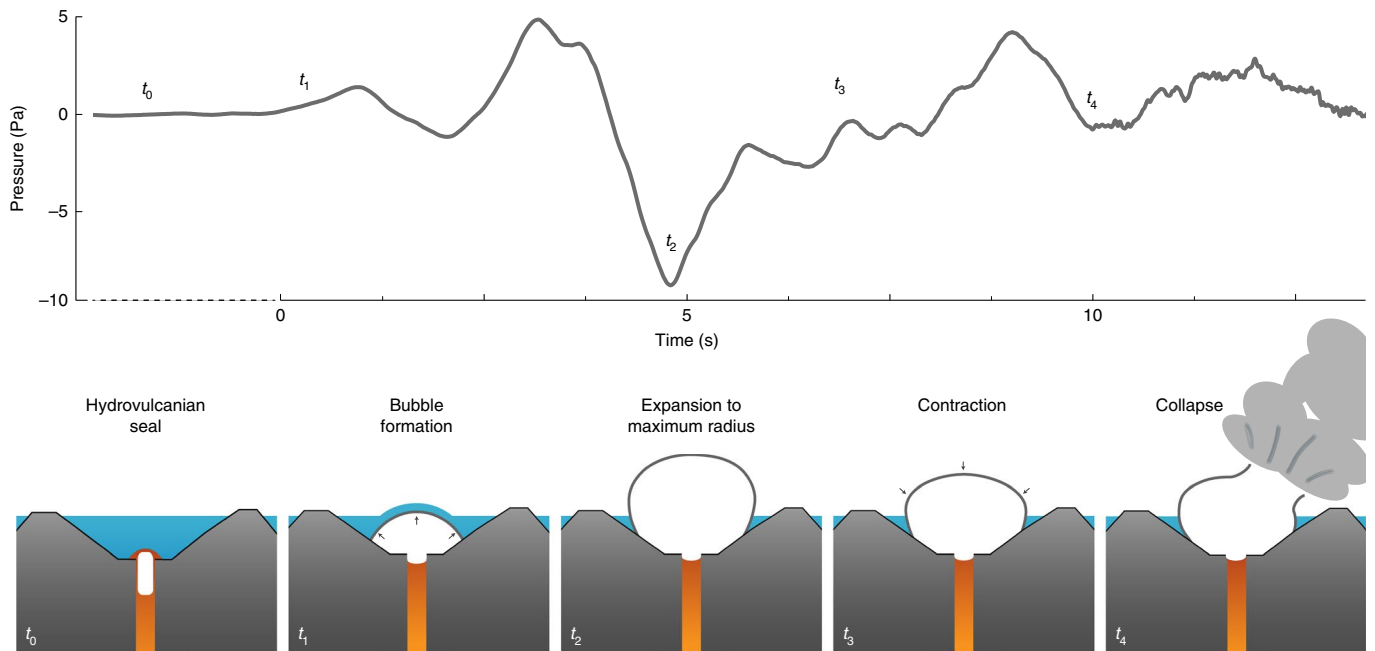
Fig. 4 | Schematic cartoon of the bubble cycle and stages of a hydrovulcanian explosion. The waveform is the event in Fig. 2c. Abundant seawater rapidly chills magma at the vent (t_0) to produce a gas-tight seal and leads to a sudden release of a large volume of pressurized gas (t_1). The resulting bubble expands through the water and into the atmosphere to reach a maximum radius (t_2) after overshooting the equilibrium radius. The bubble then begins to contract and undershoots the equilibrium radius (t_3). As the contracting bubble nears the minimum radius, it becomes unstable, which leads to rupture (t_4), gas venting and seawater interaction at the vent that produced the observed eruption clouds.

(equation (4)) and solved it with a Runge–Kutta ordinary differential equation solver (Methods). We considered that the synthetic waveforms matched the observed events if they fell within ±5% of the observed signal peak-to-peak pressure and dominant frequency (Fig. 3a). This approach produced a subset of synthetic waveform matches for all 262 observed events, with a minimum of 36, maximum of 1,213 and mean of 332 model fits to the data. We then took the mean values from each subset to determine the best-fit bubble parameters for each observed event, with the s.d. of each parameter for the subset indicating the variability (Supplementary Fig. 1). This approach resulted in non-unique solutions to the bubble parameters for each event but, as the starting conditions were difficult to constrain for Bogoslof, these results better sample the model space and provide a general insight into the bubble source parameters. Overall, the results tend to span the initial conditions for each parameter without clustering near endmember values, which indicates that the ranges of initial conditions are acceptable. The average bubble radius, water depth, source pressure and fluid film thickness are 115 m, 46 m, 1.32×10^6 Pa and 0.44 m, respectively (Fig. 3 and Supplementary Fig. 1).

The results show that, in general, the bubble parameters vary proportionally when compared to the observed pressure and dominant frequency (Fig. 3). This is not surprising as the modelled frequency of oscillation is a function of the size of the source and thickness of the fluid layer, and the amplitudes are a function of the pressure in the bubble. In particular, the low-frequency character of the Bogoslof infrasound signals requires extremely large source bubbles. However, some events fall off the main trend, for example, several of the 17 February and 13 June 2017 events (Supplementary Fig. 1b). These events have the lowest observed pressures, which suggests that path effects may have reduced the amplitudes of these signals and thus the bubble size and volume are underestimated. Our model does not account for propagation of the infrasound between source and receiver (Methods). Atmospheric conditions

are highly variable in this part of Alaska and can change rapidly, which potentially affects signal character at the source–receiver distance of our data[49].

This model for sound production is highly non-linear when large oscillations are considered and results in an asymmetry between the positive and negative peaks in pressure[25], similar to the asymmetry in the waveforms in Fig. 2. The oscillation history of a model bubble begins with expansion that continues until the maximum radius is reached, which coincides with the minimum radiated pressure as the acceleration and velocity of the bubble cap reach minima (Fig. 4). Contraction of the bubble follows and proceeds through the equilibrium radius until the minimum radius is achieved after one full oscillation (Fig. 4). Under ideal conditions, the model bubble then repeats the sequence, but the observed low-frequency waveforms indicate that typically only a single oscillation of the bubble cap occurs before it becomes unstable (Figs. 2 and 4). The high-frequency signal in the Bogoslof data increases in amplitude just after the model predicts a maximum contraction of the bubble cap, which indicates that the bubble became unstable, ruptured and vented pressurized gas (Fig. 4). Bubble collapse is typically caused by irregularities that develop in the spherical shape as the bubble contracts[43]. Such irregularities arise from a number of factors not considered in the modelling here, which include interaction with other bubbles, proximity to hard surfaces (like crater walls) and gravitational drainage of the fluid in the bubble cap[31,43,50]. Although consideration of these factors is beyond the scope of this work, they probably explain some of the observed variations in the low-frequency waveforms, particularly during contraction (Figs. 2 and 4).

The large source bubbles predicted by the Bogoslof signals result in gas volumes per bubble from 2.62×10^5 to 2.22×10^7 m³, with an average volume of 5.08×10^6 m³ (Fig. 3c). These volumes are significantly larger than those calculated for weak strombolian activity at Erta ′Ale (36–700 m³) (ref. [40]), as well as for typical

strombolian activity at Stromboli (10–2×10^4 m³) (refs. [25,51,52]), Shishaldin (1×10^4 m³) (ref. [31]) and Etna (5×10^5 m³) (ref. [26]). However, they overlap with the volume estimates for more energetic explosions at Sakurajima (1.1×10^5–1.2×10^7 m³) (ref. [53]) and for a paroxysmal eruption at Stromboli (5.7×10^5 m³) (ref. [54]). Thus, the large volumes of gas released in the Bogoslof events are consistent with an energetic explosive source, in agreement with other eruption observations, which include widely observed infrasound and seismic signals[55], volcanic lightning[28], eruption clouds up to 12 km above sea level and evidence of widespread ballistic fallout and pyroclastic flow deposits across the subaerial portion of the island.

Model of hydrovulcanian explosions

Seawater that flooded the vent during nearly all the Bogoslof eruptive events almost certainly influenced the eruptive style; however, the contribution of seawater flashing to steam in the overall gas budget that produced the giant bubbles was probably small. The efficiency of explosive steam generation in magma–water interactions depends on sufficient magma fragmentation to rapidly transfer magmatic heat to the water[56]. At water/magma mass ratios greater than one, magma fragmentation, the production of superheated steam and explosivity begin to decrease[57]. Thus, in cases like Bogoslof, in which the mass of available seawater greatly exceeds the mass of magma, the volume of magmatic gas available at the timescale of individual explosive events should be much higher than the volume of steam created.

Explosive hydrovolcanism, often described as surtseyan, is characterized by multiple tephra jets and is frequently associated with billowing steam clouds[58]. However, in all the descriptions of large bubbles that grow and rupture during shallow subaqueous eruptions, the tephra jets and steam appear after the bubbles have grown to their maximum size and are associated with the rupture and disintegration of the well-formed bubble[12,13,45,48]. This chronology suggests that the gas phase is largely separated from the magma, and that when the bubble collapses, seawater can more readily interact with the magma to produce hydromagmatic explosions, surtseyan-style jets or sustained tephra-steam emissions.

We propose that the more profound role of seawater in eruptions like Bogoslof is its ability to rapidly quench the magma carapace at the vent to produce a gas-tight seal. The abundant water allows the repeated production of this seal, which traps shallowly exsolving gas[11] or ascending gas slugs[25,26,31] just below the vent (Fig. 4). The accumulation of overpressurized gas leads to the brittle failure of the magma and rapid release of the large volumes of gas responsible for the giant bubbles. The sequences of closely spaced explosive eruptions at Bogoslof are therefore similar to vulcanian explosions[59], but able to repeat on much shorter timescales because the water-cooled magma quickly seals degassing pathways: we refer to this activity as hydrovulcanian.

Impressive accumulations of ballistic ejecta were associated with many of the eruptive episodes and much of this ejecta consists of dense, poorly vesicular basaltic andesite and trachybasalt, probably derived from shallow submarine cryptodomes. Thus, we suggest that multiple lava domes were built and destroyed during the 2016–2017 Bogoslof eruption, only a few of which reached the surface and extended above water[27]. Our results indicate that the unique infrasound signals produced by Bogoslof were a sign of the submarine effusion of gas-rich magma, and that similar signals may be expected from other shallow subaqueous volcanoes across a range of magma compositions.

Online content

Any methods, additional references, Nature Research reporting summaries, source data, statements of code and data availability and associated accession codes are available at https://doi.org/10.1038/s41561-019-0461-0.

References

1. Mastin, L. G. & Witter, J. B. The hazards of eruptions through lakes and seawater. *J. Volcanol. Geotherm. Res.* **97**, 195–214 (2000).
2. Embley, R. W. et al. Long-term eruptive activity at a submarine arc volcano. *Nature* **441**, 494–497 (2006).
3. White, J. D. L., Smellie, J. L. & Clague, D. A. in *Explosive Subaqueous Volcanism* (eds White, J. D. L., Smellie, J. L. & Clague, D. A.) 1–23 (American Geophysical Union, 2013).
4. Green, D. N. et al. Hydroacoustic, infrasonic and seismic monitoring of the submarine eruptive activity and sub-aerial plume generation at South Sarigan, May 2010. *J. Volcanol. Geotherm. Res.* **257**, 31–43 (2013).
5. Fiske, R. S., Cashman, K. V., Shibata, A. & Watanabe, K. Tephra dispersal from Myojinsho, Japan, during its shallow submarine eruption of 1952–1953. *Bull. Volcanol.* **59**, 262–275 (1998).
6. Kano, K. in *Explosive Subaqueous Volcanism* (eds White, J. D. L., Smellie, J. L. & Clague, D. A.) 213–229 (American Geophysical Union, 2013).
7. Wohletz, K. H. Explosive magma–water interactions: thermodynamics, explosion mechanisms, and field studies. *Bull. Volcanol.* **48**, 245–264 (1986).
8. Schipper, C. I. & White, J. D. L. Magma–slurry interaction in Surtseyan eruptions. *Geology* **44**, 195–198 (2016).
9. Ichihara, M. et al. Airwaves generated by an underwater explosion: implications for volcanic infrasound. *J. Geophys. Res.* **114**, B03210 (2009).
10. Zimanowski, B., Büttner, R., Lorenz, V. & Häbulletifele, H.-G. Fragmentation of basaltic melt in the course of explosive volcanism. *J. Geophys. Res.* **102**, 803–814 (1997).
11. Morrissey, M., Gisler, G., Weaver, R. & Gittings, M. Numerical model of crater lake eruptions. *Bull. Volcanol.* **72**, 1169–1178 (2010).
12. Morimoto, R. & Ossaka, J. The 1952–1953 submarine eruption of the Myojin Reef near the Bayonnaise Rocks, Japan. *Tokyo Univ. Earthq. Res. Inst. Bull.* **33**, 221–250 (1955).
13. Belousov, A. & Belousova, M. in *Volcaniclastic Sediment. Lacustrine Settings* (eds White, J.D.L. & Riggs, N. R.) 35–60 (Wiley, 2009).
14. Thorarinsson, S. *The Surtsey Eruption: Course of the Events and the Development of the New Island*. Surtsey Research Progress Report 1 (Surtsey Research Society, 1965).
15. Watts, A. B. et al. Rapid rates of growth and collapse of Monowai submarine volcano in the Kermadec Arc. *Nat. Geosci.* **5**, 510–515 (2012).
16. Metz, D., Watts, A. B., Grevemeyer, I., Rodgers, M. & Paulatto, M. Ultra-long-range hydroacoustic observations of submarine volcanic activity at Monowai, Kermadec Arc. *Geophys. Res. Lett.* **43**, 1529–1536 (2016).
17. Cole, R. H. *Underwater Explosions* (Princeton Univ. Press, 1948).
18. Kedrinskii, V. K. *Hydrodynamics of Explosion: Experiments and Models* (Springer, 2005).
19. Fee, D. & Matoza, R. S. An overview of volcano infrasound: from Hawaiian to Plinian, local to global. *J. Volcanol. Geotherm. Res.* **249**, 123–139 (2013).
20. Johnson, J. B. & Ripepe, M. Volcano infrasound: a review. *J. Volcanol. Geotherm. Res.* **206**, 61–69 (2011).
21. Godin, O. A. Anomalous Transparency of water–air interface for low-frequency sound. *Phys. Rev. Lett.* **97**, 164301 (2006).
22. Evers, L. G. et al. Evanescent wave coupling in a geophysical system: airborne acoustic signals from the Mw 8.1 Macquarie Ridge earthquake. *Geophys. Res. Lett.* **41**, 1644–1650 (2014).
23. Ripepe, M. & Gordeev, E. Infrasonic waves and volcanic tremor at Stromboli. *Geophys. Res. Lett.* **23**, 181–184 (1996).
24. Rowe, C. A., Aster, R. C., Kyle, P. R., Dibble, R. R. & Schlue, J. W. Seismic and acoustic observations at Mount Erebus volcano, Ross Island, Antarctica, 1994-1998. *J. Volcanol. Geotherm. Res.* **101**, 105–128 (2000).
25. Vergniolle, S. & Brandeis, G. Strombolian explosions: 1. A large bubble breaking at the surface of a lava column as a source of sound. *J. Geophys. Res.* **101**, 20433 (1996).
26. Vergniolle, S. & Ripepe, M. From Strombolian explosions to fire fountains at Etna Volcano (Italy): what do we learn from acoustic measurements? *Geol. Soc. Lond. Spec. Publ.* **307**, 103–124 (2008).
27. Coombs, M. L. et al. Short-term forecasting and detection of explosions during the 2016–2017 eruption of Bogoslof volcano, Alaska. *Front. Earth Sci.* **6**, 122 (2018).
28. Haney, M. M. et al. Volcanic thunder from explosive eruptions at Bogoslof volcano, Alaska. *Geophys. Res. Lett.* **45**, 3429–3435 (2018).
29. Olson, J. V. & Szuberla, C. A. L. Distribution of wave packet sizes in microbarom wave trains observed in Alaska. *J. Acoust. Soc. Am.* **117**, 1032–1037 (2005).
30. Johnson, J. B., Aster, R. C. & Kyle, P. R. Volcanic eruptions observed with infrasound. *Geophys. Res. Lett.* **31**, L14604 (2004).
31. Vergniolle, S., Boichu, M. & Caplan-Auerbach, J. Acoustic measurements of the 1999 basaltic eruption of Shishaldin volcano, Alaska: 1. Origin of Strombolian activity. *J. Volcanol. Geotherm. Res.* **137**, 109–134 (2004).

32. Lighthill, J. *Waves in Fluids* (Cambridge Univ. Press, 1978).
33. Vergniolle, S. & Brandeis, G. Origin of the sound generated by Strombolian explosions. *Geophys. Res. Lett.* **21**, 1959–1962 (1994).
34. Johnson, J., Aster, R., Jones, K. R., Kyle, P. & McIntosh, B. Acoustic source characterization of impulsive Strombolian eruptions from the Mount Erebus lava lake. *J. Volcanol. Geotherm. Res.* **177**, 673–686 (2008).
35. Gerst, A., Hort, M., Aster, R. C., Johnson, J. B. & Kyle, P. R. The first second of volcanic eruptions from the Erebus volcano lava lake, Antarctica—energies, pressures, seismology, and infrasound. *J. Geophys. Res. Solid Earth* **118**, 3318–3340 (2013).
36. Johnson, J. B. & Miller, A. J. C. Application of the monopole source to quantify explosive flux during vulcanian explosions at Sakurajima Volcano (Japan). *Seismol. Res. Lett.* **85**, 1163–1176 (2014).
37. Firstov, P. P. & Kravchenko, N. M. Estimation of the amount of explosive gas released in volcanic eruptions using air waves. *Volcanol. Seismol.* **17**, 547–560 (1996).
38. Simojoki, H. On seiches in some lakes in Finland. *Geophysica* **7**, 145–150 (1961).
39. Garcés, M. et al. Infrasound from large surf. *Geophys. Res. Lett.* **33**, L05611 (2006).
40. Bouche, E. et al. The role of large bubbles detected from acoustic measurements on the dynamics of Erta ʹAle lava lake (Ethiopia). *Earth Planet. Sci. Lett.* **295**, 37–48 (2010).
41. Kobayashi, T., Namiki, A. & Sumita, I. Excitation of airwaves caused by bubble bursting in a cylindrical conduit: experiments and a model. *J. Geophys. Res. Solid Earth* **115**, B10201 (2010).
42. Plesset, M. S. & Prosperetti, A. Bubble dynamics and cavitation. *Annu. Rev. Fluid Mech.* **9**, 145–185 (1977).
43. Leighton, T. G. *The Acoustic Bubble* (Academic, 1994).
44. Lu, N. Q., Oguz, H. N. & Prosperetti, A. The oscillations of a small floating bubble. *Phys. Fluids A Fluid Dyn.* **1**, 252–260 (1989).
45. Cheminée, J. L. et al. Gas-rich submarine exhalations during the 1989 eruption of Macdonald Seamount. *Earth Planet. Sci. Lett.* **107**, 318–327 (1991).
46. Rubin, K. H. & Macdougall, J. D. Submarine magma degassing and explosive magmatism at Macdonald (Tamarii) seamount. *Nature* **341**, 50–52 (1989).
47. Waythomas, C. F. & Cameron, C. *Historical Eruptions and Hazards at Bogoslof Volcano Alaska U.S.* Science Investigation Report 2018-5085 (US Geological Survey, 2018).
48. Prosser, W. T. Nature turned sorceress. *Tech. World Mag.* **XV**, 64–68 (1911).
49. Iezzi, A.M., Schwaiger, H. F., Fee, D. & Haney, M. Application of an updated atmospheric model to explore volcano infrasound propagation and detection in Alaska. *J. Volcanol. Geotherm. Res.* **371**, 192–205 (2018).
50. Krieger, J. R. & Chahine, G. L. Acoustic signals of underwater explosions near surfaces. *J. Acoust. Soc. Am.* **118**, 2961–2974 (2005).
51. Ripepe, M. & Marchetti, E. Array tracking of infrasonic sources at Stromboli volcano. *Geophys. Res. Lett.* **29**, 33-1–33–4 (2002).
52. Chouet, B. et al. Source mechanisms of explosions at Stromboli Volcano, Italy, determined from moment–tensor inversions of very-long-period data. *J. Geophys. Res. Solid Earth* **108**, ESE 7-1–ESE 7-25 (2003).
53. Fee, D. et al. Eruption mass estimation using infrasound waveform inversion and ash and gas measurements: evaluation at Sakurajima Volcano, Japan. *Earth Planet. Sci. Lett.* **480**, 42–52 (2017).
54. Ripepe, M. & Harris, A. Dynamics of the 5 April 2003 explosive paroxysm observed at Stromboli by a near-vent thermal, seismic and infrasonic array. *Geophys. Res. Lett.* **35**, L07306 (2008).
55. Wech, A., Tepp, G., Lyons, J. & Haney, M. Using earthquakes, T waves, and infrasound to investigate the eruption of Bogoslof Volcano, Alaska. *Geophys. Res. Lett.* **45**, 6918–6925 (2018).
56. Wohletz, K., Zimanowski, B. & Büttner, R. in *Modeling Volcanic Processes: The Physics and Mathematics of Volcanism* (eds Fagents, S. A., Gregg, T. K. P. & Lopes, R. M. C.) 230–257 (Cambridge Univ. Press, 2013).
57. Sheridan, M. F. & Wohletz, K. H. Hydrovolcanic explosions: the systematics of water–pyroclast equilibration. *Science* **212**, 1387–1389 (1981).
58. Kokelaar, B. P. The mechanism of Surtseyan volcanism. *J. Geol. Soc. Lond.* **140**, 939–944 (1983).
59. Clarke, A. B.in *Modeling Volcanic Processes: The Physics and Mathematics of Volcanism* (eds Fagents, S. A., Gregg, T. K. P. & Lopes, R. M. C.) 129–152 (Cambridge Univ. Press, 2013); https://doi.org/10.1017/CBO9781139021562.007

Acknowledgements

Author contributions

J.J.L., M.M.H., D.F. and A.G.W. initiated the study and guided the investigation. J.J.L. and M.M.H. processed the data and performed the numerical modeling. A.G.W. and J.J.L. produced the map in Fig. 1a and C.F.W. processed the images for Fig. 1b,c. J.J.L. wrote the manuscript with input from all the co-authors.

Competing interests

The authors declare no competing interests.

Additional information

Methods

Data. The Alaska Volcano Observatory (AVO) monitors volcanic activity with a network of single-station infrasound sensors co-located with seismic stations and six multi-element sensor arrays at distances of 15–250 km from most active volcanoes in the arc (www.avo.alaska.edu/about/infrasound.php). The infrasound array closest to Bogoslof is located 59 km south on Okmok volcano (Fig. 1a) and had four elements arranged in a ~100 m aperture triad around a central element. We present data from only this array because it recorded more of the eruptive events with greater fidelity than any of the more distal arrays. The entire catalogue of events recorded at the OKIF array is available in Wech et al.[55]. All the AVO arrays recorded eruption infrasound from Bogoslof at one time or another, out to distances of over 800 km, but not all of the arrays detected all of the eruptions. Changes in the dominant wind direction and atmospheric temperature profile over the course of the eruption resulted in variability as to which arrays detected each eruption. Infrasound data at Okmok were recorded continuously at 100 Hz on a Quanterra Q330S digitizer and the array was equipped with Chaparral 25Vx sensors that had a flat frequency response from 0.1 to the 50 Hz Nyquist frequency, a linear full-scale output of ±360 Pa, and a sensitivity of 50 mV Pa^{-1}. The nearest seismic stations were over 45 km away and are part of the volcano monitoring networks on the Umnak and Unalaska islands (Fig. 1a).

Acoustic source models. Volcano acoustic sources have often been modelled as a linear combination of monopoles, dipoles and quadrupoles. The volumetric oscillation of a gas bubble near a fluid–air boundary results in a monopole acoustic source in the air[25,44]. A monopole is a simple acoustic source that radiates sound equally in all directions, and in volcanic systems can arise from a rapid, isotropic gas expansion or a time-varying volume flux into the atmosphere[32]. This has led to monopole source approximations for impulsive signals from discrete explosions at multiple volcanoes[34,60,61] and provides a simple method to estimate volume flux[37]. However, this method does not consider the effects of topography or atmospheric structure, which can strongly affect the acoustic waveform and may result in incorrect volume fluxes[62]. A second type of simple acoustic source is the dipole, which involves no net volume flux and can be represented by two closely spaced monopoles that act in opposite phase[32]. Dipole sources result from momentum changes in the fluid that disturb the atmosphere and have directional radiation patterns that require characterization with observations from multiple azimuths around the source[35,63]. The combination of two dipoles produces a third type of acoustic radiation, the quadrupole. Quadrupole radiation is often associated with volcanic jets and fumaroles[64–66] and is a less efficient source of sound because it exerts no net force or net volume flux on the atmosphere[32]. The large distance from Bogoslof to the OKIF infrasound sensors (59 km) and the discrete character of the waveforms make it highly unlikely that the recorded signals contain a significant quadrupole component.

Detailed studies of infrasound from explosive eruptions at Mount Erebus[34,35] and Tungurahua[63] recently presented evidence of multipole radiation, with a contribution from both monopole and dipole radiation. At Tungurahua the dipole component arises primarily from the interaction of rapidly expanding gas with complex crater geometries, whereas at Erebus the dipole component is proposed to be generated by an initial asymmetric rupture of the bubble and associated directional jet that transitions into a monopole as the rupture expands. The Bogoslof eruptions emanated from the sea with no topography to affect the waveforms (Fig. 1), and thus the production of a large dipole component by this method is unlikely. No images or video of the Bogoslof eruptions were captured, but the increase in high-frequency energy in the waveforms suggests that no significant jetting occurred until after one full cycle of oscillation (Fig. 2c,d). To resolve accurately the contribution of each component through source inversion requires multiple stations at different azimuths, and ideally within 15 km of the vent[62,63]. Our Bogoslof observations were typically recorded at a single array at 59 km, which provided no information on the source directionality and relative contributions of the monopole, dipole or quadrupole. Other studies primarily relied on signal character[67,68] or independent observations of plume characteristics[69,70] to constrain the dominant radiation. For example, continuous, longer-lived (55–350 s) vulcanian eruptions at Augustine Volcano were analysed as a pure dipole source from a steady gas jet that interacted with solid crater walls and ash particles[68]. Compared to the Augustine explosions, the energetic portion of the Bogoslof events modelled here are of short duration (3–10 s) and discrete, with only one low-frequency cycle per event (Fig. 2c,d). Thus, the waveform characteristics, lack of topography and limited, distal observations together support the approximation of the Bogoslof source as a simple monopole.

Volume expansion and burst monopole source model. The idealized bursting of a pressurized sphere produces an isotropic expansion and N-shaped waveform where the period of the waveform τ is a function of the radius of the sphere R_s and the speed of sound in the atmosphere c (refs. [32,33]):

$$\tau = 2R_s/c \tag{1}$$

The low-frequency infrasound signals from Bogoslof have periods down to 8.3 s, which for a sound speed of 340 m s^{-1} results in a source radius of 1,411 m. This is unrealistically large given the ~250–350 m maximum crater radii observed

during the Bogoslof eruption (Fig. 1). The low-frequency Bogoslof signals also lack the rapid rise time characteristic of N-shaped waves[71,72]. More generally, a volumetric expansion can be described as a monopole source in which the source area is compact and small relative to the wavelength of the resulting infrasound. The excess acoustic pressure $\Delta P(r,t)$ as a function of time t for a volume $V(t)$ expanding from the water surface is then[32]:

$$\Delta P(r, t) = \frac{\rho_{atm}}{2\pi r}\frac{d^2}{dt^2}[V(t - r/c)] \tag{2}$$

where r is the distance from the vent (5.9×10^4 m) and atmospheric density ρ_{atm} is 1 kg m^{-3}. The volume flux is then the integral of excess pressure, and the cumulative volume flux is the twice-integrated excess pressure. This method is particularly sensitive to long-period period pressure changes, so it should be suited to the Bogoslof signal. However, the results can also be influenced by instrument drift or filter artefacts, and so we follow the method of Johnson and Miller[36] to condition the waveform to help account for possible spurious long-period noise. We also deconvolved the instrument response, but did not apply a filter (Supplementary Figs. 2 and 3). The dominant rarefaction in the waveform results in a net negative cumulative flux, even after applying the detrending correction[36]. This is not physically plausible given that a volcanic eruption explosively injects material into the atmosphere.

Seiche source model. Long-period standing waves, or seiches, can be generated in semi-enclosed bodies of water by numerous natural sources, which include earthquakes[73], calving glaciers[74] and potentially by underwater volcanic explosions. The Merian formula relates the dimensions of the body of water with the period of the standing waves τ (ref. [75]):

$$\tau = \frac{2L}{\sqrt{gd}} \tag{3}$$

where L is the longest dimension of the body of water, d is the mean water depth and g is the acceleration of gravity (9.8 m s^{-2}). The range of crater dimensions from satellite observations of Bogoslof's crater (300–500 m) and likely water depths (5–100 m) from the National Oceanic and Atmospheric Administration bathymetry (see above) produce dominant periods of 20–100 s, or much longer than the 8.3 s period infrasound signals from Bogoslof.

Bubble oscillation monopole model. The general equation for bubble motion as a result of the exchange of kinetic energy between the thin bubble cap and potential energy of the gas is[25]:

$$0 = \ddot{\varepsilon} + \left(\frac{12\mu_l}{\rho_l R_{eq}^2}\right)\dot{\varepsilon} + \frac{P_{atm}}{\rho_l R_{eq} h_{eq}}\left[1 - \left(\frac{V_{eq}}{V_g}\right)^\gamma\right](1 + \varepsilon)^2 \tag{4}$$

where V_{eq} and R_{eq} are the bubble equilibrium volume and radius, respectively, the atmospheric pressure P_{atm} is 10^5 Pa, the liquid density ρ_l and viscosity μ_l are set to standard seawater values of 1,030 kg m^{-3} and 0.01 Pa s, and the volume of gas in the bubble V_g is a function of dimensionless bubble radius ε. The pressure inside the bubble will vary with changes in its volume because heat transfer within large bubbles is adiabatic[42]. The ratio of specific heat γ is set to 1.1 because the gases in the bubble are presumed to be hot[32]. The bubble radius R can be represented by the variation from its equilibrium radius R_{eq}:

$$R = R_{eq}(1 + \varepsilon) \tag{5}$$

where

$$R_{eq} = \left(\frac{3}{2}\right)^{\frac{1}{3}}\left[\left(\frac{2R_o^3}{3} + \frac{2R_o^2 L}{3}\right)\left(1 + \frac{\Delta P}{P_{atm}}\right)^{\frac{1}{\gamma}} - \frac{2R_o^2 D}{3}\right]^{\frac{1}{3}} \tag{6}$$

and in which R_o is the starting radius of the bubble, D is the depth of water above the vent and ΔP is the source pressure, or amount the bubble initially at rest at the air–water boundary is suddenly overpressured. We set the initial radial velocity to zero when solving equation (4), which corresponds to a newly formed bubble near its minimum radius prior to oscillation[31].

The model assumes that a bubble initially at rest is suddenly overpressurized by ΔP. This results in the growth and oscillation of the bubble, and we can track the resulting changes in pressure and volume because they are adiabatic processes. Atmospheric pressure waves in the model are produced by the motion of the thin layer of liquid driven by changes in gas pressure within the bubble. The pressure recorded at the sensor $P_{ac} - P_{atm}$ at time t is[25,32]:

$$P_{ac} - P_{atm} = \frac{d^2}{dt^2}\left[\frac{2\pi R^3\left(t - \frac{r}{c}\right)}{3}\right]\frac{\rho_{atm}}{2\pi r} \tag{7}$$

where P_{ac} is the source pressure, r is 5.9×10^4 m and c is 340 m s^{-1}. In cases where the starting radius exceeds the depth of the water, the shape of the submerged volume becomes an oblate hemispheroid. The total volume of the bubble V_g is then the

volume of the hemisphere that expands from the water surface into the atmosphere plus the hemispheroid volume in the water column:

$$V_g = \frac{2\pi R^3}{3} + \frac{2}{3}\pi R_o^2 D \qquad (8)$$

The calculation of synthetic pressure histories thus primarily depends on four variables: ΔP, R_o, D and h_{eq}. We set the initial bubble overpressure range to 10^4–5×10^6 Pa to encompass the range of the maximum signal pressures recorded at 59 km (0.2–21 Pa) and assumed attenuation from geometric spreading only. Modelling of atmospheric and topographic effects on infrasound amplitudes at similar source–receiver distances shows that, together, these effects can cause the observed signals to be smaller or larger than the predicted signals by up to an order of magnitude[76]. Although topography is minimal in this case, the effects of atmospheric wind and temperature variations cannot be properly evaluated because atmospheric data in this remote area currently lack the resolution required[49]. Future work is needed to fully account for path effects at these midrange regional distances (10–100 km).

Some advantages to recording energetic explosions at these distances are that monopole radiation dominates and non-linear effects that may strongly affect near-field records are minimized[77]. We lack information on vent geometry, but fix the vent radius to 25 m based on models of similar systems[11]. The range of initial bubble radii thus varies from the vent radius, 25 m, to 200 m, or slightly smaller than the approximate radius of the crater area around the time of the observed signals (Fig. 1b,c). In our model, large bubbles most probably formed at or near the vent in the base of the shallow submerged crater (Fig. 4), and thus the height of the submerged portion of the bubble is controlled by the depth of the water. Variations in the depth of water above the vent over the course of the eruption are poorly constrained, although pre-eruption bathymetry shows depths of 100 m or less in the vent region. For simplicity, the range of water depths was set at half of the range of initial bubble radii, or 12–100 m. The most challenging parameter to constrain is the thickness of the fluid shell over the gas bubble, which plays a role in determining source pressure because the fluid layer is the mass of the oscillator[31]. Previous models of gas bubbles oscillating in magma used fluid thicknesses of 0.1–0.4 m, largely based on the average diameter of tephra ejected during strombolian activity[25,40]. Given the lower density and viscosity of sea water compared to magma, and the energetics of the eruption, we chose 0.1–1 m as the range of thicknesses for the fluid layer.

Data availability

Observations of volcanic activity were made by AVO and are detailed on its website (www.avo.alaska.edu/volcanoes/volcinfo.php?volcname=Bogoslof). The infrasound data analysed in this study are available for download from the IRIS-DMC (http://ds.iris.edu/mda/AV/) or from the corresponding author upon request.

References

60. Albert, S., Fee, D., Firstov, P., Makhmudov, E. & Izbekov, P. Infrasound from the 2012–2013 Plosky Tolbachik, Kamchatka fissure eruption. *J. Volcanol. Geotherm. Res.* **307**, 68–78 (2015).
61. Dalton, M. P., Waite, G. P., Watson, I. M. & Nadeau, P. A. Multiparameter quantification of gas release during weak Strombolian eruptions at Pacaya Volcano, Guatemala. *Geophys. Res. Lett.* **37**, L09303 (2010).
62. Kim, K., Fee, D., Yokoo, A. & Lees, J. M. Acoustic source inversion to estimate volume flux from volcanic explosions. *Geophys. Res. Lett.* **42**, 5243–5249 (2015).
63. Kim, K., Lees, J. M. & Ruiz, M. Acoustic multipole source model for volcanic explosions and inversion for source parameters. *Geophys. J. Int.* **191**, 1192–1204 (2012).
64. Matoza, R. S., Fee, D., Neilsen, T. B., Gee, K. L. & Ogden, D. E. Aeroacoustics of volcanic jets: acoustic power estimation and jet velocity dependence. *J. Geophys. Res. Solid Earth* **118**, 6269–6284 (2013).
65. McKee, K., Fee, D., Yokoo, A., Matoza, R. S. & Kim, K. Analysis of gas jetting and fumarole acoustics at Aso Volcano, Japan. *J. Volcanol. Geotherm. Res.* **340**, 16–29 (2017).
66. Woulff, G. & McGetchin, T. R. Acoustic noise from volcanoes: theory and experiment. *Geophys. J. R. Astron. Soc.* **45**, 601–616 (1976).
67. Vergniolle, S. & Caplan-Auerbach, J. Basaltic thermals and subplinian plumes: constraints from acoustic measurements at Shishaldin volcano, Alaska. *Bull. Volcanol.* **68**, 611–630 (2006).
68. Caplan-Auerbach, J., Bellesiles, A. & Fernandes, J. K. Estimates of eruption velocity and plume height from infrasonic recordings of the 2006 eruption of Augustine Volcano, Alaska. *J. Volcanol. Geotherm. Res.* **189**, 12–18 (2010).
69. Ripepe, M. et al. Ash-plume dynamics and eruption source parameters by infrasound and thermal imagery: the 2010 Eyjafjallajökull eruption. *Earth Planet. Sci. Lett.* **366**, 112–121 (2013).
70. Delle Donne, D. & Ripepe, M. High-frame rate thermal imagery of strombolian explosions: implications for explosive and infrasonic source dynamics. *J. Geophys. Res. Solid Earth* **117**, B09206 (2012).
71. Kinney, G. F. & Graham, K. J. *Explosive Shocks in Air* 2nd edn (Springer, 1985).
72. Morrissey, M. M. & Chouet, B. A. Burst conditions of explosive volcanic eruptions recorded on microbarographs. *Science* **275**, 1290–1293 (1997).
73. Ichinose, G., Anderson, J. G., Schweickert, R. A. & Lahren, M. M. The potential hazard from tsunami and seiche waves generated by large earthquakes within Lake Tahoe, California–Nevada. *Geophys. Res. Lett.* **27**, 1203–1206 (2000).
74. Walter, F., Olivieri, M. & Clinton, J. F. Calving event detection by observation of seiche effects on the Greenland fjords. *J. Glaciol.* **59**, 162–178 (2013).
75. Rueda, F. J. & Schladow, S. G. Surface seiches in lakes of complex geometry. *Limnol. Oceanogr.* **47**, 906–910 (2002).
76. Lacanna, G. et al. Influence of atmospheric structure and topography on infrasonic wave propagation. *J. Geophys. Res. Solid Earth* **119**, 2988–3005 (2014).
77. Pierce, A. D. *Acoustics—An Introduction to Its Physical Principles and Applications* (McGraw-Hill, 1981).